Montanuniversität Leoben

Synthesis of α–$(Al,Cr)_2O_3$ solid solution coatings with different Al/(Al+Cr) ratios by pulsed DC magnetron sputtering

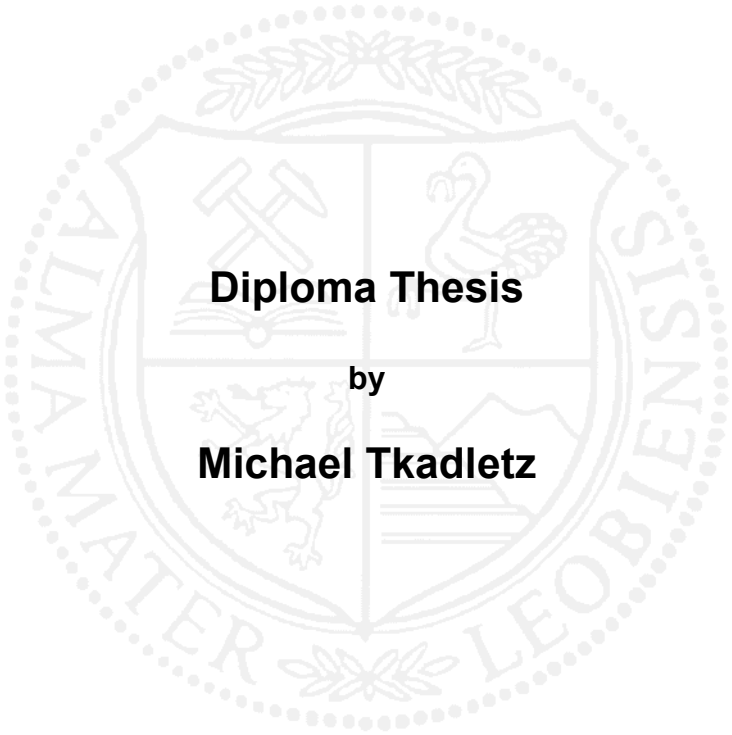

Diploma Thesis

by

Michael Tkadletz

This work has been carried out within the Research Studio Austria Surface Engineering at the Chair of Functional Materials and Material Systems, Montanuniversität Leoben, Austria.

Leoben, November 2011

Affidavit

I declare in lieu of oath, that I wrote this thesis and performed the associated research myself, using only literature cited in this volume.

Leoben, November 2011

Acknowledgments

My sincerest gratitude is due to Univ. Prof. DI Dr. Christian Mitterer, head of the Chair of Functional Materials and Material Systems, for his supervision, the patience and the confidence he placed in me.

I would also like to express my thankfulness to DI Nina Schalk for her patience and great support while supervising me at writing this thesis.

Furthermore, I am very grateful to DI Viktoria Edlmayr who helped me a lot carrying out the depositions for this work.

I would also like to thank PLANSEE Composite Materials and CERATIZIT Austria, for providing the targets and substrates for this work.

Also, I would like to thank the entire Thin Film Group for the great support whenever needed and the pleasurable working atmosphere.

Finally, I want to thank my parents. I am deeply grateful for all the support and love they are giving to me.

Table of Contents

Page

1 Introduction

Thin films are well established for corrosion and wear protection, in microelectronics as diffusion barriers and for other components in mechanical engineering. The use of coated cutting tools instead of conventional ones makes increased cutting speeds possible and leads to less tool wear. Thus, the efficiency and the range of machineable materials can be enhanced [1].

In the previous years, alumina (α–Al_2O_3) has gained increasing interest due to its favourable properties like corrosion resistance, high temperature hardness and as diffusion barrier [2]. Al_2O_3 exists in a number of crystallographic modifications, with the thermodynamically stable α–Al_2O_3 beeing the most wanted one. The deposition of alumina by chemical vapor deposition (CVD) methods is well established since years, but it is not very suitable for heat sensitive substrate materials, due to the high deposition temperatures of about 1000 °C [3]. In contrast to CVD, the deposition temperatures using physical vapor deposition (PVD) are much lower (400 to 700 °C). The deposition of Al_2O_3 utilizing PVD leads in general to amorphous or thermodynamically metastable crystallographic modifications, but there are several approaches to deposit alumina using PVD. One concept is to deposit a solid solution consisting of Al_2O_3 and Cr_2O_3, where the Cr_2O_3, which has the same crystallographic structure as alumina, stimulates growth of alumina.

In the present work, segmented sputter targets have been used to deposit $(Al,Cr)_2O_3$ coatings with different Al/(Al+Cr) ratios, depending on the position of the sample on the substrate holder. The aim was to determine crystallographic structure, residual stresses and mechanical as well as tribological properties depending on the aluminum content in the film.

2 Thin Film Synthesis

2.1 Physical Vapor Deposition

Thin films provided by PVD are well established in e.g. tribological applications, for microelectronics and for optical devices. The PVD process can be divided into three major steps [4]:

1. Transition from the solid target material to the gas phase
2. Transport of the evaporated target material to the substrate surface
3. Adsorption, nucleation and growth of the evaporated target material on the substrate surface

The way how the target material is evaporated leads to a further classification of PVD into [4]:

- Vacuum Evaporation (thermal evaporation using e.g. an arc discharge)
- Sputtering (evaporation by bombarding the solid target material with gas ions)
- Ion Plating (thermal evaporation followed by an ionization of the target material)

Using PVD almost every kind of inorganic material (e.g. metals, alloys, compounds) can be deposited on a wide range of substrate materials (e.g. metals, plastics, glass). Chemical compounds can be deposited by adding a reactive gas into the recipient or by using compound targets. Also several organic materials can be deposited [5, 6]. The main benefits of PVD are the variety of possible film and substrate materials, the possibility of low deposition temperatures and the excellent bonding between film and substrate [4].

2.2 Sputtering

The transition of the solid target material to the gas phase by bombarding the target surface with energetic ions is called sputtering (Fig. 2.1). There, a working gas, like e.g. Ar is fed into the recipient. By applying a voltage between target and substrate, where the target acts as cathode and the substrate as anode, a plasma is ignited. The working gas atoms are ionized and can be accelerated to the target by applying a negative offset voltage. Interactions between impinging ions and target atoms can lead to direct ejection of a target atom or to ejection caused by collision cascades, if the energy transferred to a surface near atom is higher than its surface binding energy. The ratio between ejected atoms and impinging ions is called sputtering

yield. Almost 99 % of the ejected particles are neutrals, thus their flight path is ballistic and cannot be influenced by magnetic or electric fields [5, 7].

Since the ejection of particles using sputtering is caused by the transfer of mechanical energy, the thermal exposure of the targets is rather low. The film growth rate is strongly dependent on the total pressure and the kinetic energy of the neutrals after ejection. Typical pressures in the recipient are between 0.1 and 1 Pa [4].

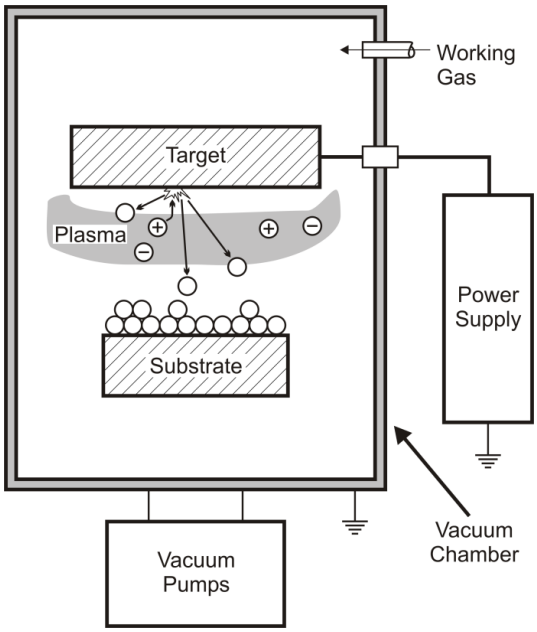

Fig. 2.1: Schematic of a sputter deposition process [6].

2.2.1 Pulsed DC Sputtering

Different types of voltages can be favorable, depending on the kind of target material which should be evaporated. When a DC voltage is applied only electrical conductors can be sputtered. Conductive, semi conductive as well as insulating materials can be used as target when a radio frequency voltage (13.56 MHz) is applied. Applying a pulsed DC voltage (10 to 100 kHz) allows the use of less conductive target materials. There, two targets can be coupled to each other and e.g. a bipolar pulsed DC voltage is applied, so that alternately one target acts as cathode and the other one as anode. The result is a downtime for the target that acts currently as anode, which leads to a reduced charging and low thermal exposure of the targets [8].

2.2.2 Unbalanced Magnetron Sputtering

In magnetron sputtering, additionaly to the electric field a magnetic field is applied in the area between the substrate and the targets. The magnetic field is generated using permanent magnets fixed behind the targets. While the ions are barely influenced by the magnetic field, the electrons get trapped in a so called race track. That causes a high electron concentration in the target near region which leads to a higher ionization rate resulting in an increase of the sputter rate. For magnetron sputtering, erosion tracks which occur under the region of the highest ionization (race track) are typical.

Unbalanced magnetron means that the magnetic field reaches the substrate surface, thus the growing film is bombarded by low energy ions and electrons caused by an increased ionization rate near the substrate surface region. This bombardment causes a higher mobility of the condensed particles on the substrate, which leads to improved film properties [9, 10].

2.2.3 Bias Sputtering

Bias sputtering means that the substrate holder is not grounded but a negative voltage called bias voltage is applied. A slightly negative potential of about -50 to -200 V relative to the plasma potential is common. Due to that negative potential, the substrate is bombarded by ions. That results in a cleaning effect and improved film growth behavior. A further improvement of bias sputtering is the pulsed bias configuration which is also needed, when insulating films are deposited, to avoid charging of the substrate. Pulsed bias can be done unipolarly or bipolarly [5, 6, 10].

2.2.4 Reactive Sputtering

An alternative to the use of compound targets to deposit compound films on a substrate is to use simple metallic targets and add a reactive gas like oxygen to the working gas. The compound of the target atoms and the reactive gas can be formed on the target surface, in the plasma or on the substrate surface. In practice the formation on the substrate surface is the most important one for compound film deposition [9, 10].

The formation of the compound on the target surface entails another effect, the so called target poisoning, which leads to a decrease of the sputter rate. Target poisoning can be shown in a hysteresis curve (Fig. 2.2) where the cathode voltage is drawn against the reactive gas flow. In the metallic state of the target, the cathode voltage is rather low and stays quite constant with increasing gas flow. At a certain point of the gas flow, the cathode voltage suddenly increases. Here the target turns into the poisoned state. This strong increase of the cathode voltage is caused by the compound which is built on the target surface and hinders sputtering. Decreasing the

reactive gas flow leads to a decrease of the cathode voltage which points out that the target returns into metallic state [11].

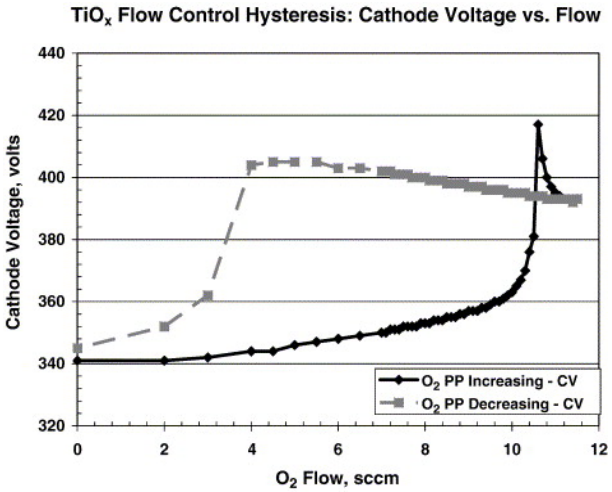

Fig. 2.2: Typical hysteresis curve in reactive sputtering [11].

2.2.5 Arcs

An issue of less conductive films is that the target gets charged while deposition due to enrichment of ions on the surface. This charge leads to a decrease of the sputtering rate and further to arcs if the potential is high enough. Those arcs damage the target and lead to contaminations. Arrangements against charging and arcs are pulsed DC or radio frequency potentials and arc suppression circuits [10].

2.3 Thin Films

2.3.1 Nucleation and Growth

Since nucleation and growth processes influence the film properties considerably, special attention has to be paid to them.

When a target material particle hits the substrate surface, the following interactions can take place (Fig. 2.3):

- The particle is reflected immediately.
- The particle is adsorbed on the surface, diffuses as so called ad-atom along the surface and desorbs again after a certain time.
- The ad-atom joins a cluster which might build a nucleus or join an existing one.

It depends on the kinetic energy of the particles which of these possibilities occur [4].

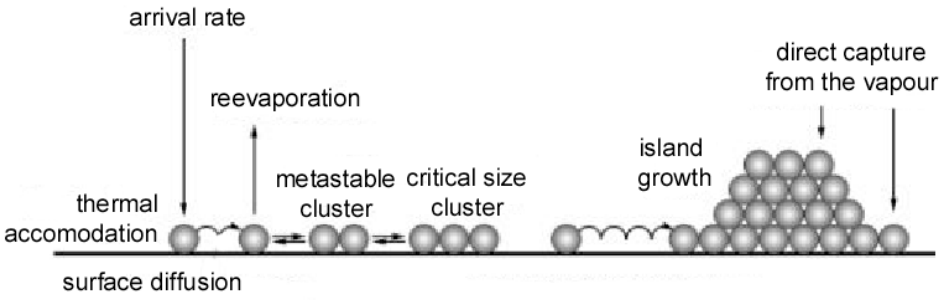

Fig. 2.3: Schematic of nucleation and growth processes [12].

Three different growth modes can be distinguished (Fig. 2.4):

- Island growth.
- Layer growth.
- Mixed growth (Island and Layer).

Island growth occurs if the binding energy between the film atoms is higher than the binding energy between substrate and film atoms. In contrast, layer growth happens if the binding energy between film and substrate atoms is higher. Mixed growth takes place if first layer growth is preferred, but then after the substrate is covered, island growth is more favorable. In general, growth is preferred at low energy sites like scratches, impurities and other defects [4].

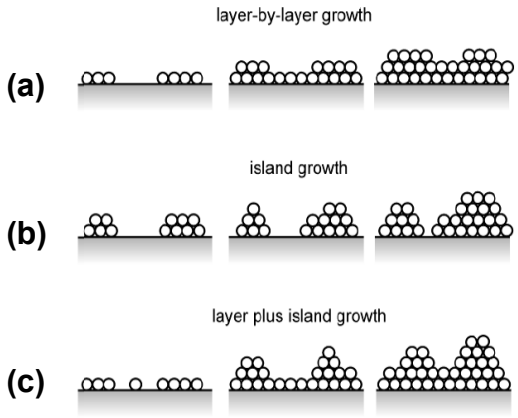

Fig. 2.4: Schematic of different growth modes: (a) layer by layer,(b) island and (c) mixed growth [13, 14].

2.3.2 Structure Zone Models (SZM)

Since there is a strong dependence of the growth behavior on the temperature, SZM´s have been developed to show these dependencies. First, Movchan and Demchishin examined vacuum evaporated films and suggested a model that depends only on the homologous temperature T/ T_M, where T denotes the substrate temperature and T_M the melting temperature of the film [15]. Later on, Thornton modified that model by adding the working gas pressure according to Fig. 2.5a. Thus, it was also applicable for sputtered films [16]. Messier *et al.* observed a dependence of the energy of the ions impinging on the substrate on the structure of the growing film (Fig. 2.5b). They revised Thornton´s model by adding the ion energy to the SZM which can be simplified described by the bias voltage [17].

In the basic SZM of Movchan and Demchishin three different zones can be distinguished. Films deposited in the first zone which ranges up to 0.26 T/ T_M show distinctive cavities and a rough surface. That is caused by the low temperature and the resulting minor movability of the adsorbed atoms on the surface. In the second zone, which reaches from 0.26 up to 0.45 T/ T_M, dense films with a smooth surface and columnar texture, caused by the higher mobility of the ad-atoms, are grown. Films grown in the third zone, which is above 0.45 T/ T_M, show a smooth surface with a dense recrystallized microstructure [15].

Thornton´s model includes an additional zone between zone one and two, called the transition zone. That transition zone shows a dense fibrous structure. The model reveals that the lower the gas pressure, the lower the temperature can be chosen to deposit a dense film, which is caused by decreasing interactions between working gas and sputtered atoms. The model also shows that for sputtered films, the film

properties can be varied in a wide range by changing working gas pressure or temperature and that sputtered films get denser at lower temperatures than arc evaporated films [16].

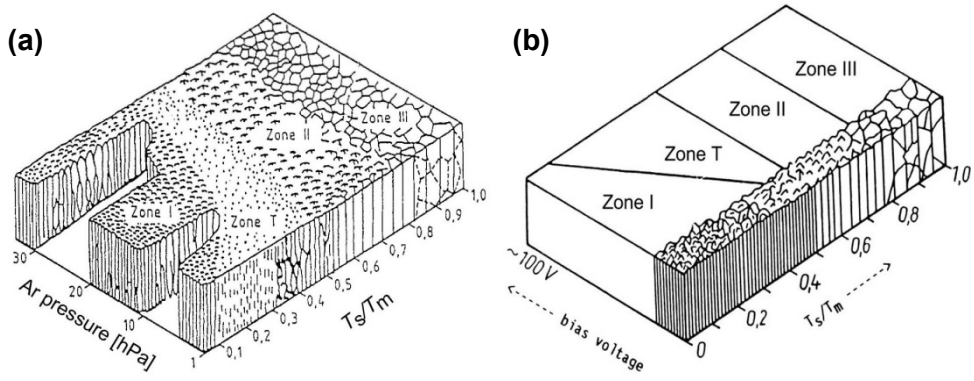

Fig. 2.5: SZM of Thornton (a) and Messier *et al.* (b) [16, 17].

The revised model of Messier *et al.* proved that the transition zone can be seen as a part of zone one. At higher bias voltages the transition zone gets broader at the expense of zone 1. That means that dense films can be deposited at rather low temperatures just by applying a higher bias voltage, which is actually caused by a higher mobility of the adatoms due to collisions with impinging ions [17].

3 Coating Materials - $(Al,Cr)_2O_3$

Aluminum oxide, Al_2O_3, is due to its excellent chemical stability in combination with its high temperature hardness and low thermal conductivity commonly used as wear and corrosion protective layer (especially at high temperatures), for diffusion barriers and in microelectronics. There are several crystallographic modifications of Al_2O_3 (e.g. α–, γ–, κ–Al_2O_3), where, due to its thermal stability, the α–modification (α–Al_2O_3, also called alumina) is the most interesting one for technical applications [18]. Alumina shows a hexagonal crystallographic structure which is also denoted as corundum or sapphire [1].

The formation of alumina films using thermal CVD is well established, but due to the high deposition temperature it is not applicable for heat sensitive substrate materials. The deposition of Al_2O_3 by PVD leads in general to the formation of amorphous Al_2O_3 or the nanocrystalline γ–modification. Since metastable γ–Al_2O_3 shows a phase transformation to the stable α–phase at temperatures of about 1000 °C [20], it is unsuitable for high temperature applications. Lattice stresses induced by that phase transition might lead to the spallation of the film.

In contrast to Al_2O_3, Cr_2O_3 always forms a stable hexagonal structure called eskolaite which is isostructural with corundum [19]. Hence, it is assumed that a single-phase $(Al,Cr)_2O_3$ film could show an improved high temperature behaviour [20].

In Fig. 3.1 the quasibinary system Al_2O_3 – Cr_2O_3 for thermal equilibrium is shown. At higher temperatures, a single corundum type phase can be seen, but at lower temperatures a large miscibility gap can be observed [21].

However, under the thermodynamical non-equilibrium conditions of PVD it has been shown that it is possible to deposit a metastable single-phase $(Al,Cr)_2O_3$ solid solution, even at lower temperatures without a limitation of the composition of the film [20].

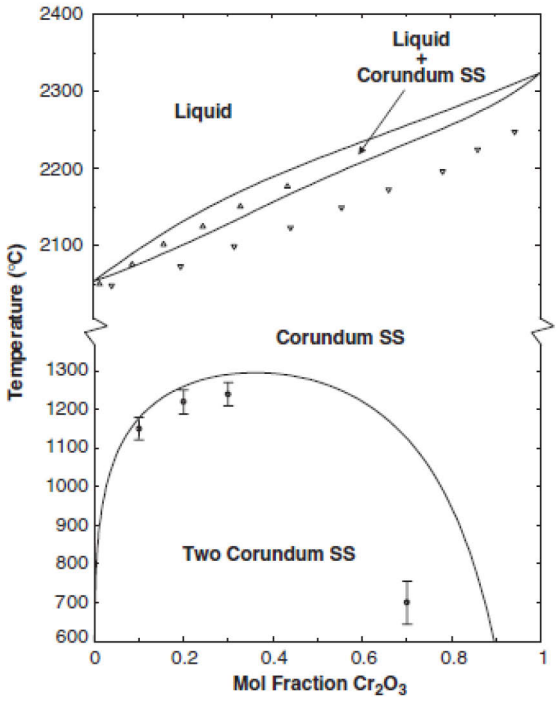

Fig.3.1: Quasibinary equilibrium phase diagram of Al_2O_3 – Cr_2O_3 [21].

Fig. 3.2 shows the lattice parameters a and c of the Al_2O_3 – Cr_2O_3 - corundum type solid solution drawn against the Al/(Al+Cr) ratio. The dotted lines connect the lattice parameters of pure α–Al_2O_3 and pure Cr_2O_3 according to Vegards law, while the rectangles mark experimental values measured by Ramm *et al*. [22].

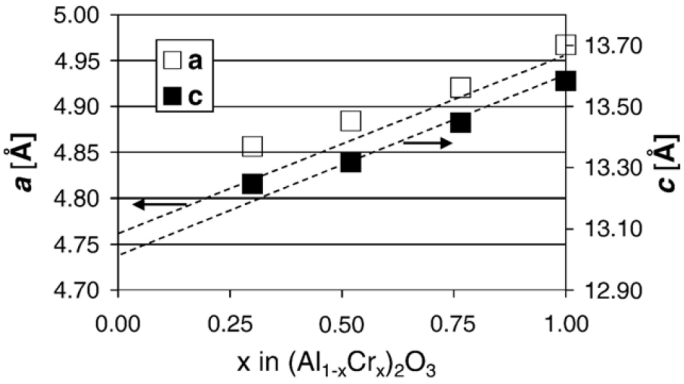

Fig.3.2: Lattice parameters of an Al_2O_3 – Cr_2O_3 solid solution [22].

4 Experimental Details

4.1 Film Deposition

4.1.1 Deposition Plant

The films presented in this work have all been deposited by reactive unbalanced magnetron sputtering with an industrial scale sputtering plant of the type CemeCon CC800® / 9MLT at the Montanuniversität Leoben. The CC800® is equipped with four bipolar pulsed DC magnetrons. Two different kinds of targets were used, (i) two standard sized (500x88x10 mm) powder metallurgically (PM) produced compound targets (Fig. 4.1a), which consist of 60 at% Al and 40 at% Ti, on one side of the recipient and (ii) on the opposite side special cathode shunts were mounted to use segmented PM targets sized 200x88x10 mm (Fig. 4.1b). Both target types were provided by PLANSEE Composite Materials in Lechbruck, Germany. The segmented targets consist of two identical triangles, one made of pure aluminum (99.5 % purity) and the other of pure chromium (99.8 % purity), which build a rectangle when they are put together. Using the segmented targets it was possible to deposit coatings with different Al/(Al+Cr) ratios, from aluminum rich to chromium rich, depending on the substrate position.

(a)

(b)

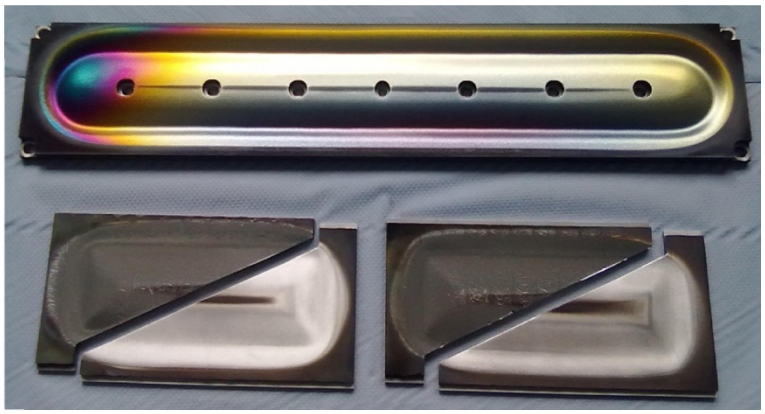

Fig. 4.1: (a) Standard sized TiAl compound target and (b) segmented Cr and Al target, respectively.

4.1.2 Substrates

Four different types of substrates were used to deposit the coatings to be investigated within this work. The coated silicon strips sized 7x21x0.38 mm were used to measure the residual stresses, to examine the crystallographic structure and to determine the hardness and the Young´s modulus of the film. The coating thickness and the film adhesion were measured on cemented carbide inserts in SNUN geometry (according to ISO 1832). Cemented carbide inserts in SEKW geometry (ISO 1832) were also coated and are preferred be used for cutting experiments, which are not part of this work. The tribological properties of the film were determined using polished cemented carbide disks with a diameter of 30 mm and a thickness of 4 mm. The cemented carbide substrates consist of 9.5 % Co, 8.6 % TiC, 10.8 % TaC and 1.2 % NbC embedded in a WC matrix.

To observe the properties of the film depending on the Al/(Al+Cr) ratio, every kind of substrate was mounted one piece upon the other on special substrate holders according to Fig. 4.2. Thus, every single sample has a different chemical composition (i.e. Al/(Al+Cr) ratio) depending on its position in relation to the targets. Altogether 15 SNUN, 16 SEKW, 28 Si plates and 3x5 tribo-discs were coated with different Al/(Al+Cr) ratios, from Cr rich to Al rich.

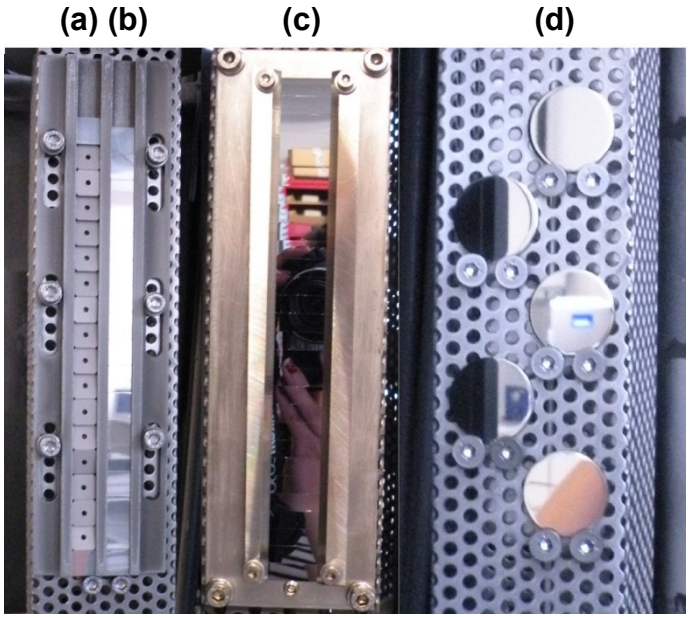

Fig. 4.2: Setup of the substrates on the substrate holder: (a) SEKW, (b) SNUN, (c) Si strips and (d) tribo discs.

4.1.3 Deposition Parameters

All samples were ultrasonically cleaned in acetone and ethanol for ten minutes each, than they were mounted on the substrate holder. Subsequently, the recipient was evacuated to a starting pressure of less than 4 mPa. Prior to deposition a heating step was done and the samples were ion etched for one hour, where the substrates are bombarded by Ar ions to clean their surface.

Then, a base layer consisting of TiAlN was deposited, using a bipolar pulsed bias voltage of -60 V and a pulse frequency of 250 kHz with a reversal time of 1600 ns. A deposition time of 5 hours was chosen to achieve an approximate film thickness of two microns. The deposition temperature was 660 °C. The gas flows were set to constant values of 150 sccm for argon and 180 sccm for nitrogen. The cathode power for the two standard TiAl targets was set to 5 kW with a pulse frequency of 20 kHz, while the segmented targets were turned off for the deposition of the base layer. Afterwards the $(Al,Cr)_2O_3$ layer was deposited. The deposition time was 12 hours and the temperature again 660 °C. The bias voltage was set to -90 V and a frequency of 350 kHz with a reversal time of 1000 ns. The gas flows were set constant to 160 sccm for argon and 240 sccm for oxygen. The cathode power for the segmented Cr and Al targets was 2.1 kW at a frequency of 50 kHz, the standard targets were turned off during the deposition of the $(Al,Cr)_2O_3$ layer.

4.2 Coating Characterization

4.2.1 Film Thickness

The film thickness was measured using the ball crater technique. There, a steel ball is covered with diamond suspension and rotated on the sample surface. Caused by that rotational movement, the steel ball grinds a calotte into the film. The inner and outer diameter of the calotte can be measured and the film thickness can be calculated [23]. A Reichert-Jung microscope of type Polyvar Met including an attached CCD camera and the analySIS® software of Soft Imaging System was used to measure these diameters. The film thickness was determined for all 15 SNUN inserts.

4.2.2 Chemical Composition

The chemical composition of the samples was measured with energy-dispersive X-ray emission spectroscopy (EDX) using a Zeiss EVO 50 scanning electron microscope (SEM) utilizing an Oxford instruments INCA extension. The implemented standards were used with a acceleration voltage of 7 kV. 15 SNUN inserts and three Si plates were analyzed.

4.2.3 Morphology and Surface Topography

The morphology and surface topography of the grown films was also examined with a Zeiss EVO 50 SEM. The surface topography of five SNUN and the film morphology of three fractured Si plates was examined.

4.2.4 Crystallographic Structure

For the characterization of the crystallographic structure, X-ray diffraction (XRD) analysis was done using a Bruker-AXS D8 Advance diffractometer. 13 Si plates as well as 15 SNUN samples were investigated in grazing incidence (GI) configuration [24]. Additionally, the samples were also investigated in Bragg-Brentano configuration [25]. They were scanned from 20° to 70° with a step size of 0.02° and a step time of 1.2 seconds. The incidence angle used for the GI-XRD measurements was 2°. The tube voltage was set to 40 kV and the tube current was 40 mA. The lattice parameters a and c were determined using the DIFFRAC^{plus} EVA software provided by Bruker AXS and the implemented ICDD standards.

4.2.5 Film Adhesion

The film adhesion was determined with a conventional Mitutoyo Rockwell C hardness tester of the type DT-10. After the indentation the damage of the surface (film) in the indentation region can be compared to a table of indents and the film adhesion can be classified from HF1 to HF6 depending on the grade of the damage [26]. For the examination of the indentations, a Reichert-Jung Polyvar Met optical microscope was used. Five SNUN samples with different Al/(Al+Cr) ratio´s were tested.

4.2.6 Residual Stresses

The quantification of the residual stresses was done using the waver curvature method. That method utilizes the effect that a waver (Si strip) which is coated on one side bends, caused by the internal stresses of the film. Two parallel laser beams with defined distance incide on the sample surface and are reflected. Due to the bending of the sample, the distance between the reflected beams is different from that of the incident beams. With this information the bending of the sample and consequently

the residual stresses can be calculated [28]. The residual stresses were determined for all 28 Si strips.

4.2.7 Hardness and Young´s Modulus

To measure the hardness and Young´s modulus of the film, a UMIS Nanoindenter (Ultra Micro Indentation System) from Fischer-Cripps Laboratories, equipped with a Berkovich indenter, was used. Since the indentation depth should be less than 10 % [27] of the film thickness, a plateau test was done from 6 to 12 mN with an increment of 0.5 mN. The mechanical properties of eleven Si strips with different Al/(Al+Cr) ratios were analyzed.

4.2.8 Tribological Properties

The tribological properties were investigated at room temperature, 500 and 700 °C by ball on disk tests using a high temperature tribometer of CSM Instruments. At every temperature five disks with different Al/(Al+Cr) ratio´s were tested. At room temperature a load of 5 N was applied, the wear track radius was 7 mm, the sliding distance 300 m and the humidity 23 %. The high temperature measurements were carried out using a load of 2 N, a wear track radius of 9 mm and a sliding distance of 6820 laps which equals a distance of 300 m at 7 mm radius. For all tests a 6 mm diameter ball made of Al_2O_3 was used.
The wear tracks were examined using a Veeco Wyko NT1000 white light interferometer in vertical scanning interferometry mode.

4.3 Calculation of the Sputtering Yield

A calculation of the sputtering yields of pure chromium and pure aluminium in a gas mixture consisting of 60 % O and 40 % Ar was done using the SRIM (**S**topping and **R**ange of **I**ons in **M**atter) simulation package [29]. The energies of the impinging ions were set to values between 200 and 1000 eV with an increment of 100 eV.

5 Results and Discussion

5.1 Chemical Composition

Every sample has a different chemical composition caused by the special geometry of the segmented targets. The oxygen content is almost constant (~58 at% Al) and stoichiometric for all samples. Thus, the following discussions are based on the metal content of the film and in particularly on the aluminum content which is denoted in atomic percent.

The chemical composition of the SNUN samples, which depends mainly on their position on the substrate holder, was determined by EDX. The aluminum content of the other sample geometries was approximated by comparing their position relative to the position of the SNUN samples on the substrate holder. Tab. 5.1 shows the positions of all samples relative to the segmented targets and their approximate aluminum content in atomic percent.

According to the target geometry, it would be expected that the Al/(Al+Cr) ratio is about 50/50 in the center region and that there is a chromium rich area on the upper side and an aluminum rich area on the lower side of the targets. In fact, the chemical analysis showed that there is much more chromium in the films than expected at all sample positions. Hence, the sputtering yields for pure chromium and pure aluminum were calculated using the SRIM simulation package [29] according to subsection 4.3. The results in Fig. 5.1 show that the sputtering yield of chromium is approximately 20 to 23 % higher than the sputtering yield of aluminum for an ion energy of 350 to 450 eV (roughly corresponding to the cathode voltage of the segmented targets of 350 to 450 V), which might be an explanation for the unexpected high chromium contents of the deposited films.

Another explanation provides the Richardsen-Ellingham diagramm [30], which shows that the standard free energy for aluminum oxide is more negative than that for chromium oxide. This indicates that aluminum oxide is more stable than chromium oxide and that more aluminum oxide than chromium oxide is built on the target surface. Hence, it can be expected that at the same time the aluminum target is partially more poisoned than the chromium target and, consequently, the conductivity of the aluminum target becomes lower, which leads to a decreased sputter rate of aluminum.

Tab. 5.1: Relationship between sample number and Al content.

Target	Al content [at%]	SNUN/SEKW	Si	Tribo disc
		Sample Nr.	Sample Nr.	Sample Nr.
Cr / Al	21.5	1	1	1
	22.9	2	2	
			3	
	24.5	3	4	
			5	
	26.8	4	6	2
			7	
	28.9	5	8	
			9	
	30.7	6	10	
			11	
	33.0	7	12	3
			13	
	35.4	8	14	
			15	
	39.0	9	16	
			17	
	38.7	10	18	4
			19	
	43.0	11	20	
			21	
	46.2	12	22	
			23	
	44.9	13	24	5
			25	
	47.3	14	26	
			27	
	48.6	15	28	

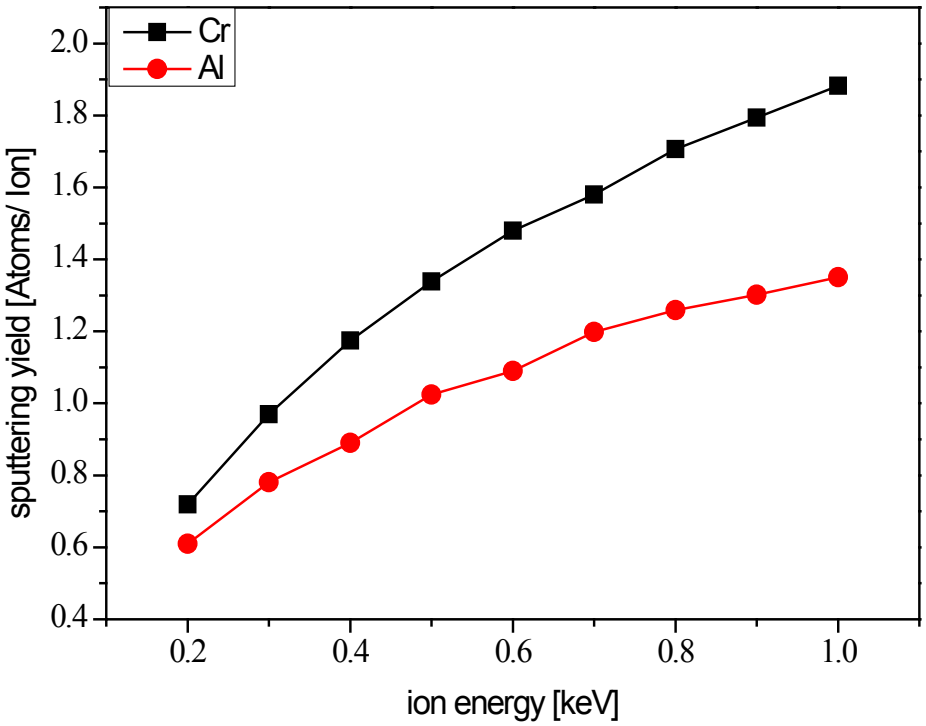

Fig. 5.1: Sputtering yield of Al and Cr in a 60/40 O/Ar mixture calculated by SRIM.

5.2 Film Thickness

According to Fig. 5.2 the film thickness is almost constant for the TiAlN baselayer, which is caused by the constant sputter conditions of the standard targets in the range of the mounted samples. The oxide film thickness shows a maximum in the central region (around 35 % Al) which equals the mid of the target height, at lower or higher aluminum contents (i.e. lower or higher sample positions) the oxide film thickness decreases.

As the upper and lower sample positions are almost in the range of the upper and lower edge of the segmented targets, the sputter conditions are not the same for the samples positioned there compared to the samples positioned in the center of the sample holder. The geometry of the erosion track (Fig. 4.1) indicates that the ion/neutral ratio is higher on the target´s upper and lower areas than in the central region. The result is a lower deposition rate on substrates positioned opposite to the lower and upper target area and consequently a lower film thickness in those regions.

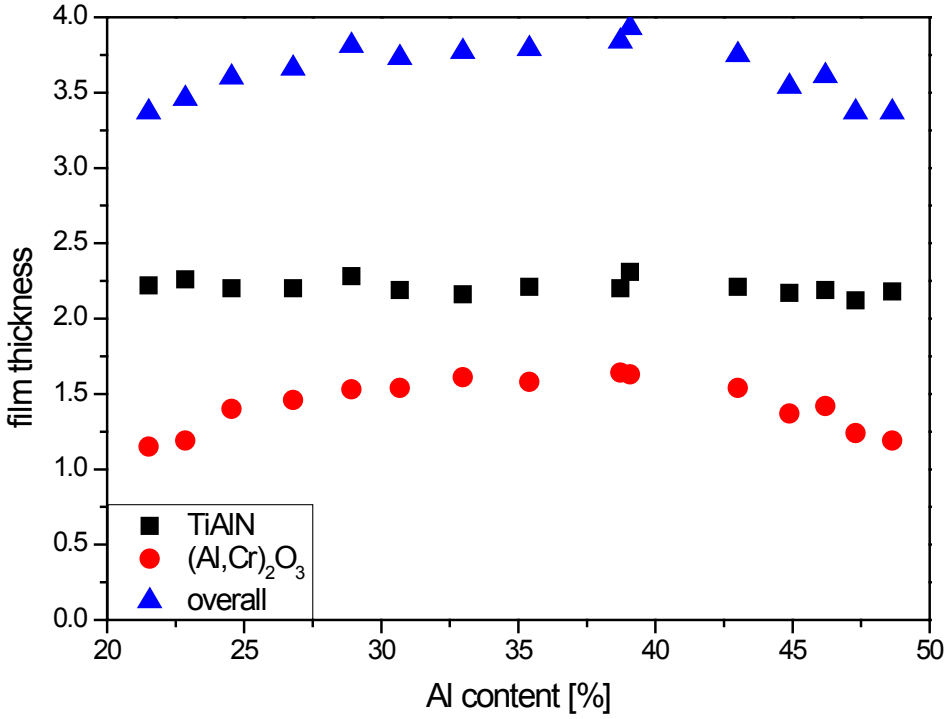

Fig. 5.2: Film thickness as a function of the Al content

5.3 Morphology and Surface Topography

In the fracture cross section of a coated Si strip (coating with 25 % Al) shown in Fig. 5.3, the ~2 μm thick TiAlN base layer and the ~1.5 μm thick $(Al,Cr)_2O_3$ layer can be identified. Both show a columnar and dense structure.

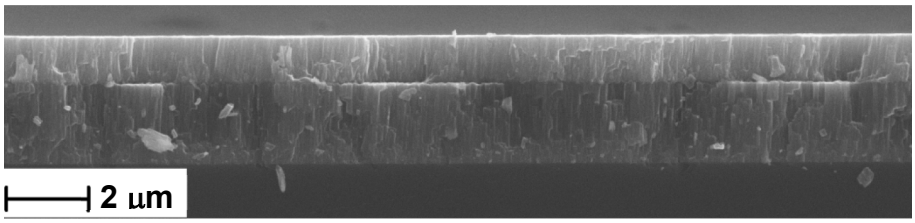

Fig. 5.3: SEM micrograph of the fracture cross section of a coated Si strip. The TiAlN base layer and the $(Al,Cr)_2O_3$ layer (25 % Al) can be identified.

The surface topography is in general quite smooth. At medium aluminum contents (Fig. 5.4b), a slight increase of the surface roughness can be observed, while it decreases at higher and lower aluminum contents (Fig.5.4a and c). That might be attributed to different etching conditions at different sample positions. At sample positions in the center of the sample holder, the erosion due to etching might be

more pronounced than at lower or higher sample positions, caused by the influence of the magnetrons on the ions in this region. The hard WC grains are not removed and consequently protrude from the surface. Due to the different etching conditions, this effect is stronger in the center of the sample holder and thus, responsible for the higher surface roughness in this region. To confirm this, in Fig. 5.5 a micrograph of the surface of a uncoated, chemically etched SNUN sample is shown, where the carbide grains can be identified.

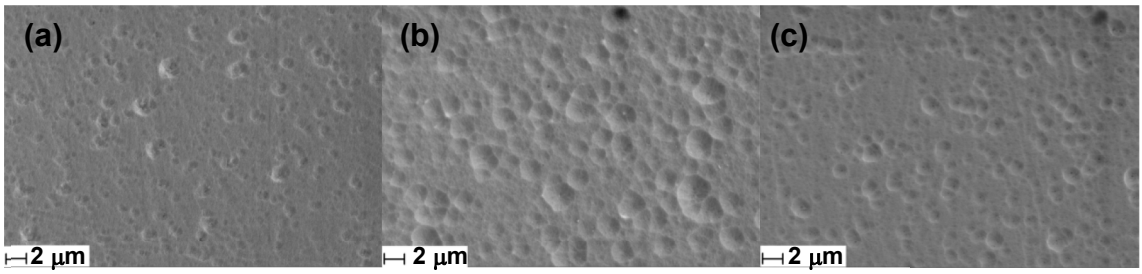

Fig. 5.4: SEM micrographs of the film surface of coated SNUN samples with (a) 22 % Al, (b) 39 % Al and (c) 49 % Al, showing different surface roughness.

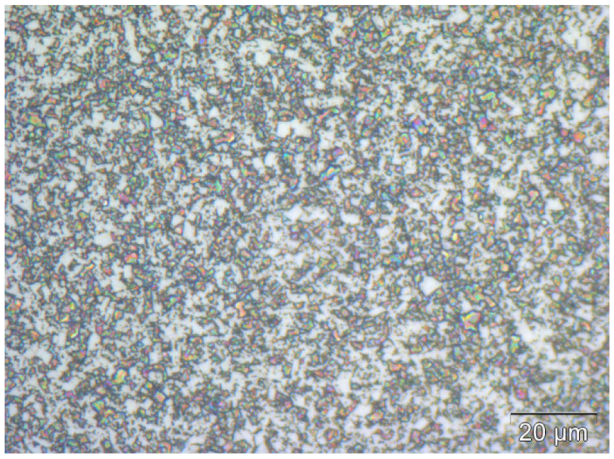

Fig. 5.5: Micrograph of the surface of an uncoated and chemically etched SNUN sample, where the carbide grains can be seen.

5.4 Crystallographic Structure

Fig. 5.5 summarizes the GI-XRD scans of seven coated Si strips with different aluminum contents, starting with the lowest aluminum content on top of the graph. The standard peak positions for α–Al_2O_3 (ICDD 00-046-1212) and Cr_2O_3 (ICDD 00-038-1479) are plotted as dashed lines in the graph. The detected peaks are located between the standard peaks of alumina and eskolaite indicating that a single phase

solid solution of $(Al,Cr)_2O_3$ is formed. No amorphous fractions or evidence for other chrystallographic phases were observed for the investigated samples. From lower to higher aluminum contents, a slight shift of the peaks from the left to the right side, i.e. from the eskolaite side to the alumina side can be observed. The texture at medium aluminum contents is more or less random distributed, while at higher and lower aluminum contents the (110) orientation is predominant. That might be a result of the increased ion bombardement at the target edge regions (compare subsection 5.2).
The evolution of the lattice parameters a and c as a function of the aluminum content is shown in Fig. 5.6. For comparison, the theoretical values calculated according to Vegard´s law are drawn as dashed lines. All determined values of the lattice constants are between those of pure alumina and pure eskolaite and decrease with increasing aluminum content according to Vegard´s law. The results are in good agreement with the values determined by Ramm *et al.* [22].

5.5 Film Adhesion

According to Fig. 5.8, the adhesion was classified as HF 5-6 (see subsection 4.2). No influence of the aluminium content on the film adhesion was detected. An accurate classification of the adherence between base layer and substrate and between base layer and oxide by examination of Fig. 5.8 is not possible. Rockwell C indentation in films deposited on substrates like cemented carbides often leads to spallation due to the high loads of ~1373 N, even if the adherence is quite well, caused by the high hardness of the substrate material. Thus, the grinded calottes which where used to measure the film thickness were also investigated regarding the coating adherence. The calotte shown in Fig. 5.9 exhibits uniform circles without spikes or chippings for both interfaces, i.e. the one between substrate and base layer and the one between base layer and oxide, which indicates, that the film adhesion is not that worse as concluded from the Rockwell indentation tests. As Weirather [31] showed, a markable improvement of the coating adherence on steel can be achieved by implementing a booster etching step between common ion etching and the coating process. This is an approach which should offer potential to improve adhesion also on cemented carbide.

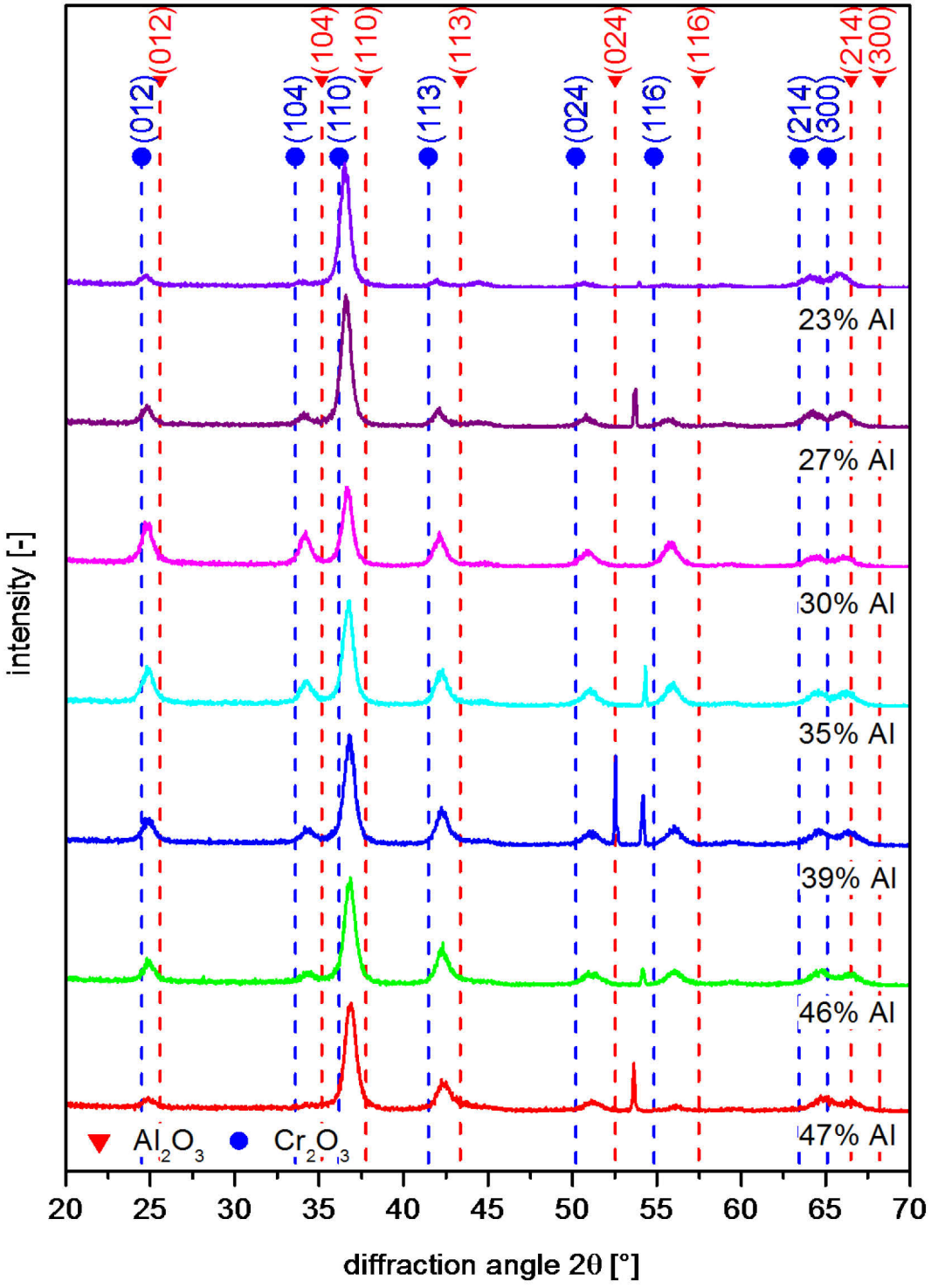

Fig. 5.6: GI-XRD scans for different Al contents measured on Si strips.

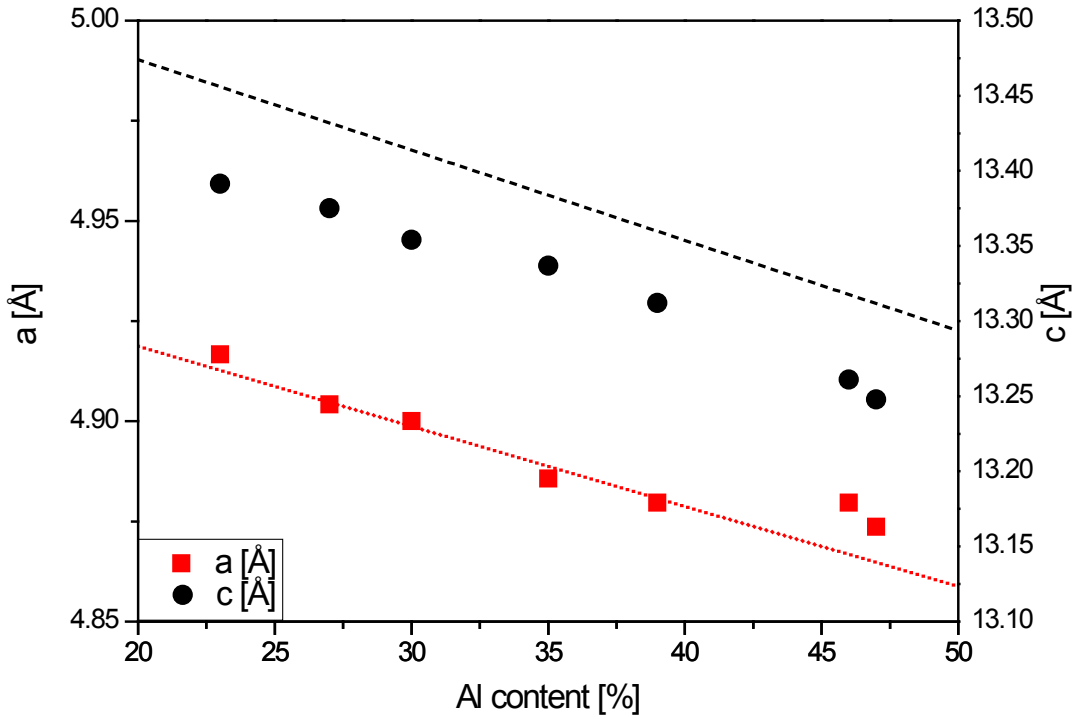

Fig. 5.7: Lattice parameters of the films as a function of the Al content.

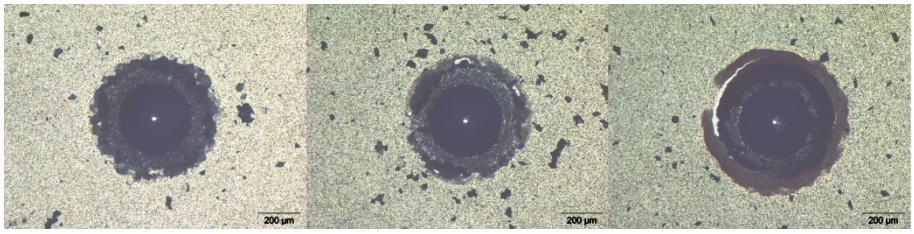

Fig. 5.8: Optical micrographs of the Rockwell C indents as examples for the adhesion of a coating with 27 % (a), 33 % (b) and 45 % (c) Al.

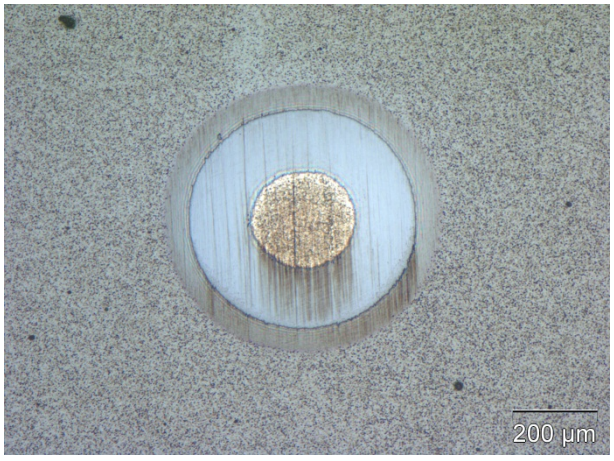

Fig. 5.9: Grinded calotte in an SNUN sample with a coating with 25 % Al. No spikes or chippings between substrate and base layer or base layer an oxide can be identfied.

5.6 Residual Stresses

All investigated samples exhibit compressive residual stresses. Fig. 5.10 shows that the compressive stresses are about -450 MPa at 22.5 % Al and decrease with increasing aluminum content to values between -200 and -100 MPa. With further increasing aluminum content the compressive stresses increase again up to -600 MPa.

As the ion/neutral ratio is higher opposite to the edges of the targets (compare subsection 5.2), the growing film is exposed to an increased ion bombardement in this area. This consequently leads to an increase of the compressive stresses in the film in this region (i.e. at lower and higher aluminum contents) [32].

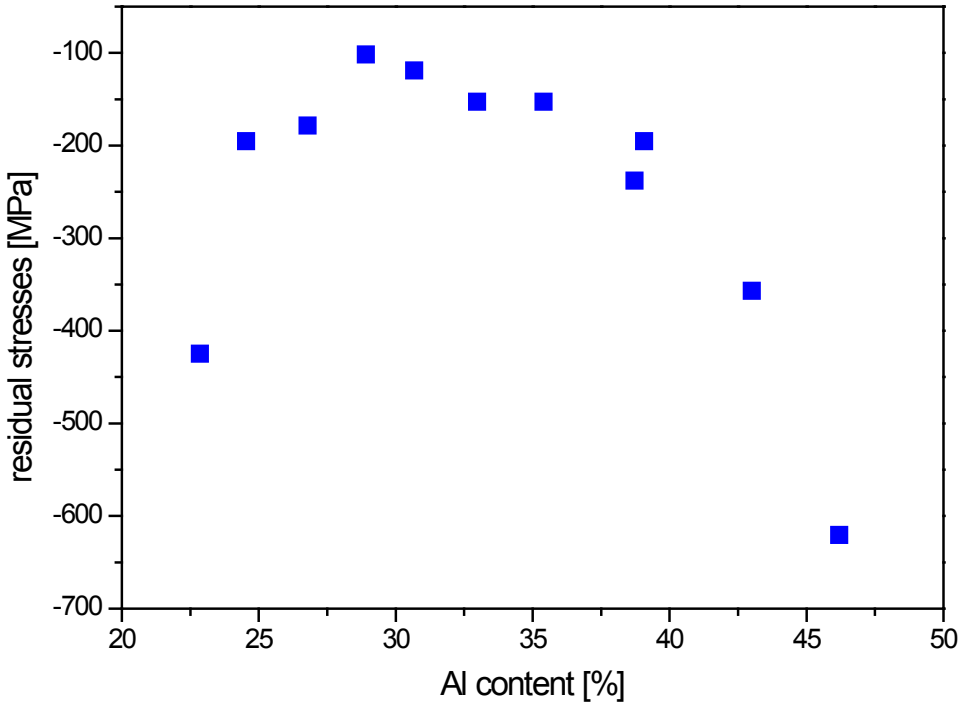

Fig. 5.10: Residual stresses in $(Al,Cr)_2O_3$ films as a function of the Al content.

5.7 Hardness and Young´s Modulus

According to Fig. 5.11, the determined hardness at lower and higher aluminum contents is higher than at medium aluminium contents. This corresponds well to the increasing compressive stresses at lower and higher aluminum contents (subsection 5.6), as coatings in general show higher hardness values with increasing compressive stresses [33]. The measured values are in good agreement with literature for other $(Al,Cr)_2O_3$ films [2, 34].

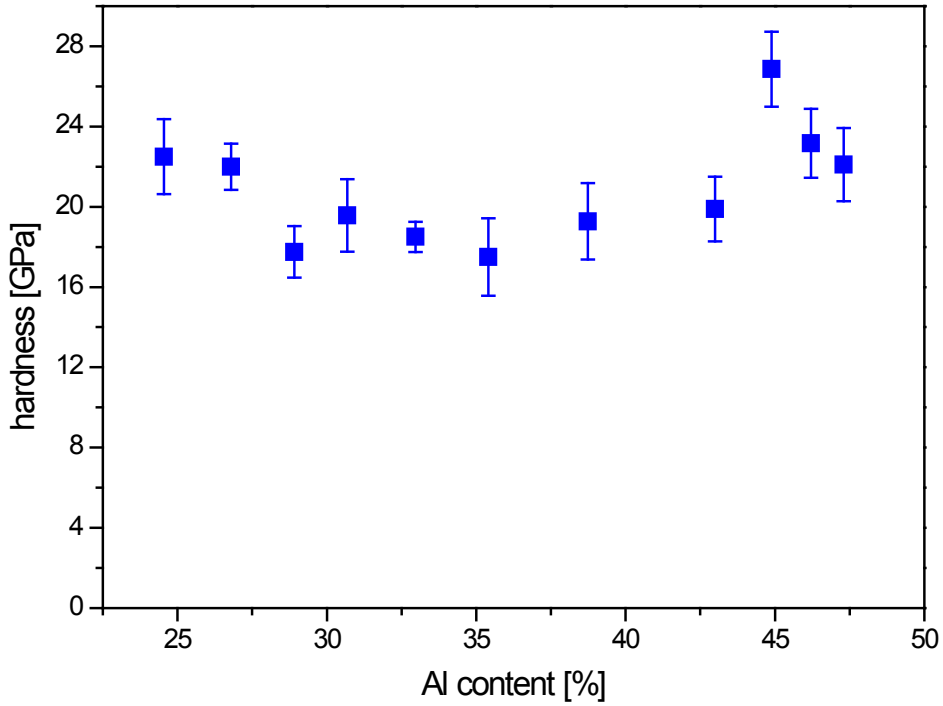

Fig. 5.11: Hardness of $(Al,Cr)_2O_3$ films as a function of the Al content measured on Si substrates.

No significant trends in dependence of the aluminum content can be observed for the Young's modulus. According to Fig. 5.12, the measured Young´s moduli range between 250 and 300 GPa. Pedersen *et al.* [35] measured values between 190 and 230 GPa for sputter deposited $(Al,Cr)_2O_3$ films with an aluminum content of ~9 to 44 %, a film thickness of 125 to 550 nm and a distinct $(10\bar{1}4)$ texture. The lower Young´s moduli might be a result of the pronounced texture. Hochauer *et al.* [36] report Young´s moduli of 330 to 450 GPa for CVD alumina films, the higher values might be caused by the deposition of pure alumina instead of a solid solution of alumina and eskolaite. Literature values for bulk alumina are between 200 and 380 GPa depending on its purity [37] which corresponds well with the values determined within this work.

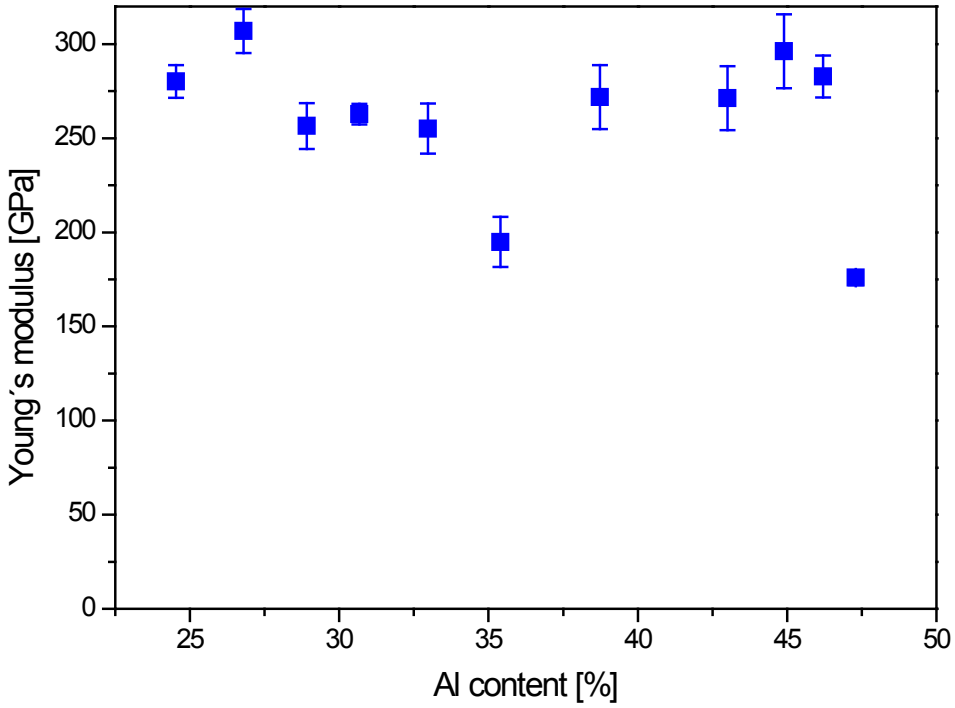

Fig. 5.12: Young´s modulus of $(Al,Cr)_2O_3$ coatings as a function of the Al content measured on Si substrates.

5.8 Tribological Properties

The coefficients of friction as a function of the sliding distance determined for coatings with different aluminum contents at room temperature are shown in Fig. 5.13. For an aluminum content of 23 %, the friction curve is quite constant and shows just small scattering. The coefficient of friction is ~0.45 ± 0.02. With increasing aluminum content, the coefficient of friction increases to ~0.89 ± 0.05 for 29 % Al and ~0.88 ± 0.02 for 35 % Al. The friction curves show an increase from a lower value at the beginning and a higher scattering when the constant value is reached. At 43 % Al the friction curve shows just small scattering and the coefficient of friction is ~0.53 ± 0.02. At 47 % Al the coefficient of friction increases from ~0.5 at the beginning up to ~0.8 at 2000 laps, then it decreases until it reaches a constant value of ~0.6 at 4500 laps. No correlation between the coefficient of friction and the aluminum content can be found at room temperature. A calculation of the wear coefficient was not possible because none of the investigated tribo discs showed a distinctive wear track. Fig. 5.14 shows a 3D image of a wear track examined with the profilometer. The wear tracks of the other samples look very similar.

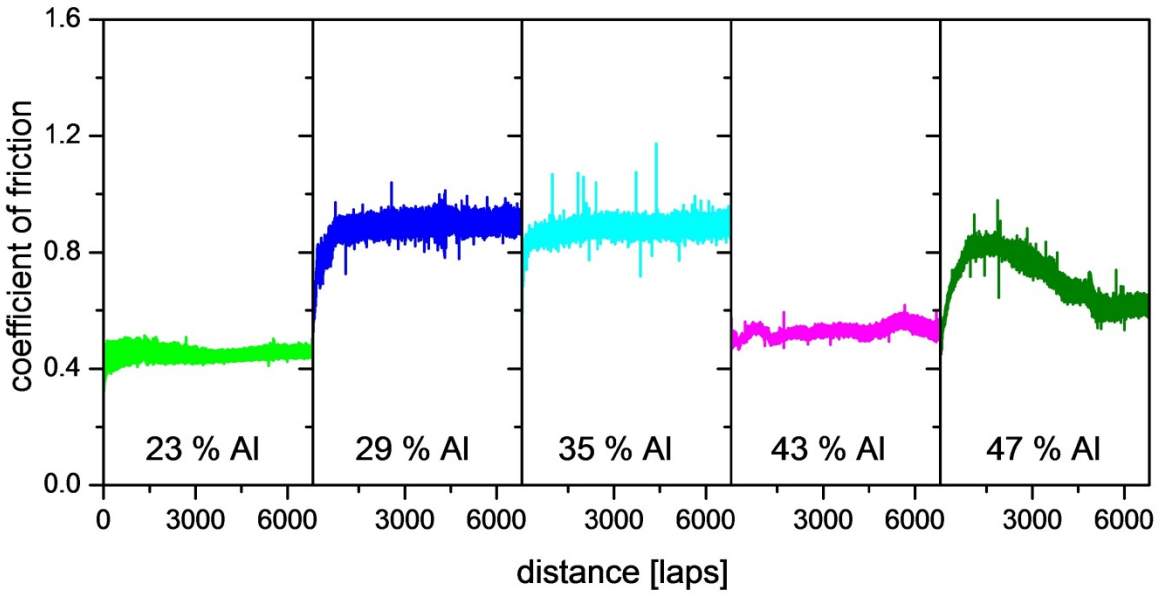

Fig. 5.13: Coefficient of friction of $(Al,Cr)_2O_3$ coatings at room temperature for different Al contents against Al_2O_3 balls.

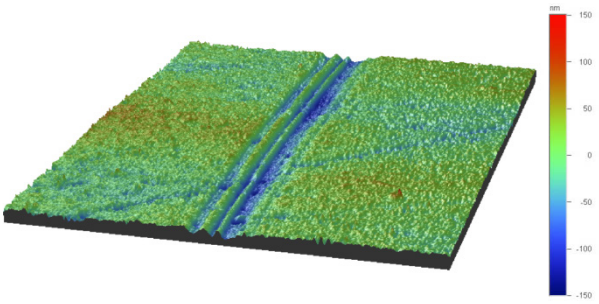

Fig. 5.14: 3D image of the investigated wear track of a tribo disc ($(Al,Cr)_2O_3$ coating with 23 % Al) tested at room temperature, showing minimal wear.

The results of the friction measurements conducted at 500 °C are presented in Fig. 5.15. The coefficient of friction increases, for all measurements, with increasing sliding distance. The steady state regime is not reached. The curves at 29, 35 and 43 % Al show high scattering and discontinuities which can be attributed to the spallation of the film. In general, a trend of an increasing coefficient of friction with increasing aluminum content, from ~0.87 ± 0.07 at 23 % Al to ~1.15 ± 0.11 at 47 % Al, can be observed.

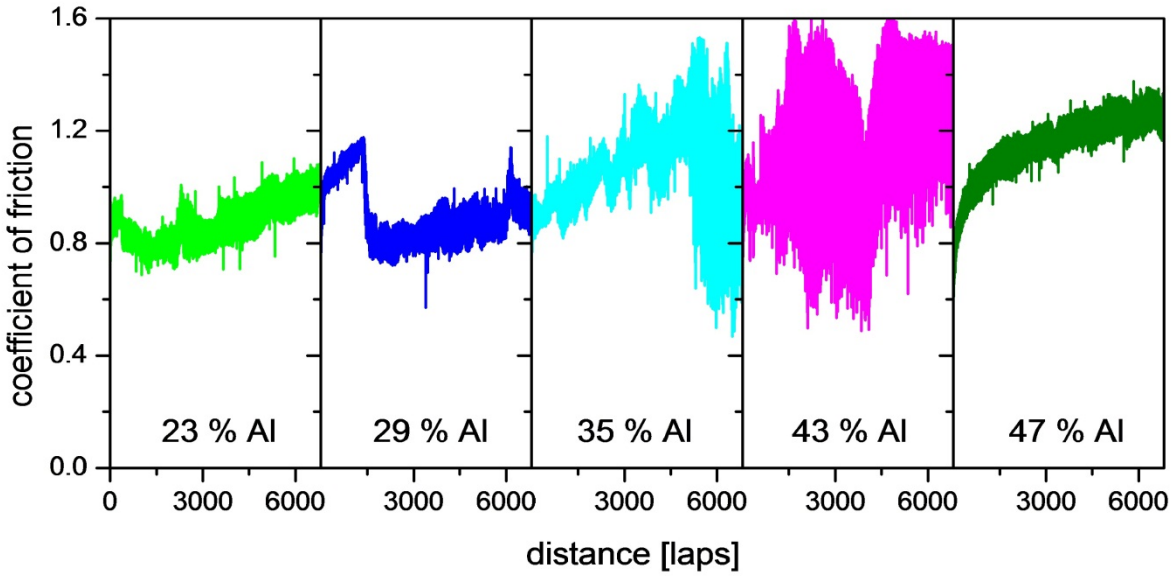

Fig. 5.15: Coefficient of friction of $(Al,Cr)_2O_3$ coatings at 500 °C for different Al contents against Al_2O_3 balls.

The examination of the wear tracks confirmed the film spallation between substrate and base layer at 29, 35 and 43 % Al, but showed no significant wear tracks at the other aluminum contents. Fig. 5.16a shows a 3D image of the wear track of a delaminated sample (29 % Al). On the borders of the wear track remains of the base layer can be identified. The sharp edge corroborates the bad adhesion classified in subsection 5.5. According Fig. 5.16 it can be assumed that the adhesion between base layer and substrate is worse than between base layer and oxide, as in the center of the wear track the almost undamaged substrate can be seen. A wear track of a film (23 % Al) with no delamination is shown in Fig. 5.16b, which exhibits wear in the magnitude of the surface roughness. Thus, also at 500 °C no wear coefficients could be calculated due to the minimal wear or the coating delamination, respectively.

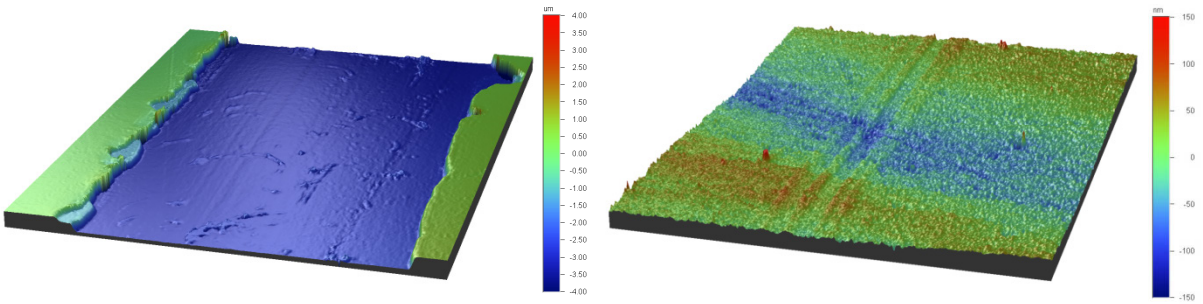

Fig. 5.16: 3D images of the investigated wear tracks of the tribo discs tested at 500 °C, showing (a) base layer delamination ($(Al,Cr)_2O_3$ coating with 29 % Al) and (b) wear in the magnitude of the surface roughness ($(Al,Cr)_2O_3$ coating with 23 % Al).

The measured friction curves at 700 °C are shown in Fig. 5.17. For coatings with 29 and 43 % Al again film spallation could be detected, which explains the scattering and discontinuities of those measurements. The other graphs show a similar behaviour like those at 500 °C, the coefficient of friction increases with increasing sliding distance and the steady state regime is not reached. With increasing aluminum content, a trend of increasing coefficients of friction from ~0.78 ± 0.11 at 23 % Al to ~1.01 ± 0.09 at 47 % Al can be observed.

At 700 °C again no distinct wear tracks were found for those curves where no delamination occurred, hence, no wear coefficients could be calculated. Fig. 5.18a shows a 3D image of the sample with 29 % Al which exhibits oxide layer delamination and wear on the nitride, while the 23 % Al sample (Fig. 5.18b) shows wear in the magnitude of the surface roughness.

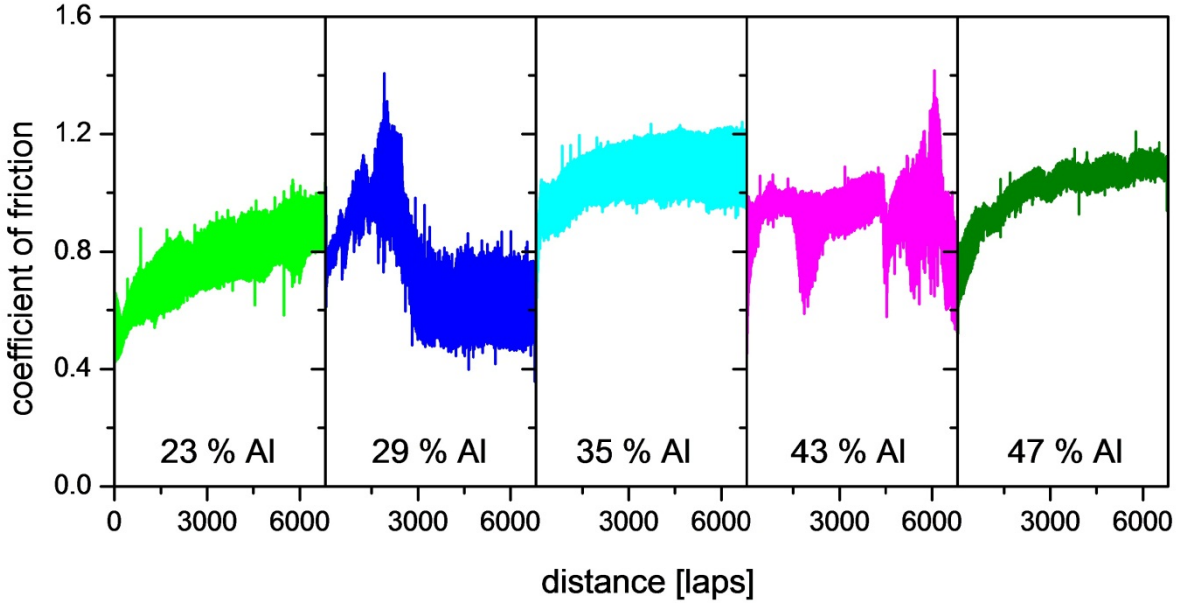

Fig. 5.17: Coefficient of friction of $(Al,Cr)_2O_3$ coatings at 700 °C for different Al contents against Al_2O_3 balls.

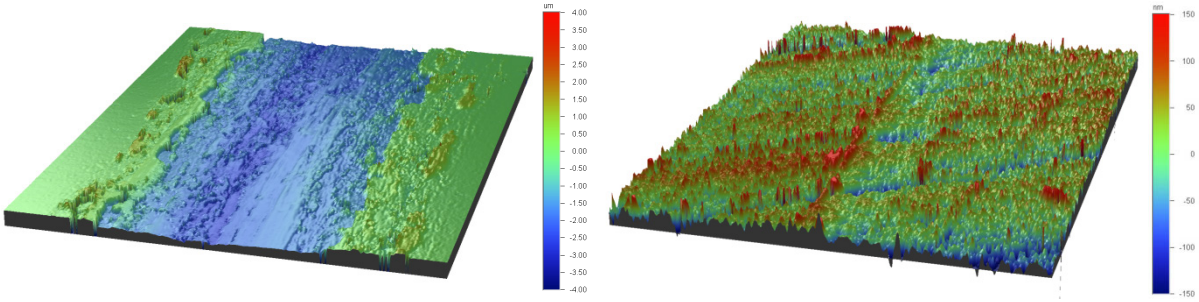

Fig. 5.18: 3D images of the investigated wear tracks of the tribo discs tested at 700 °C, showing (a) oxide delamination and wear on the nitride ($(Al,Cr)_2O_3$ coating with 23 % Al) and (b) minimal wear in the magnitude of the surface roughness ($(Al,Cr)_2O_3$ coating with 29 % Al).

Fig.5.19 summarizes the coefficients of friction obtained for room temperature, 500 and 700 °C. It shows no unambiguous trend for the values measured at room temperature. At 500 and at 700 °C an increasing coefficient of friction with increasing aluminum content can be observed. The values measured at 500 °C are slightly higher than those measured at 700 °C. The lowest coefficients of friction are measured at room temperature.

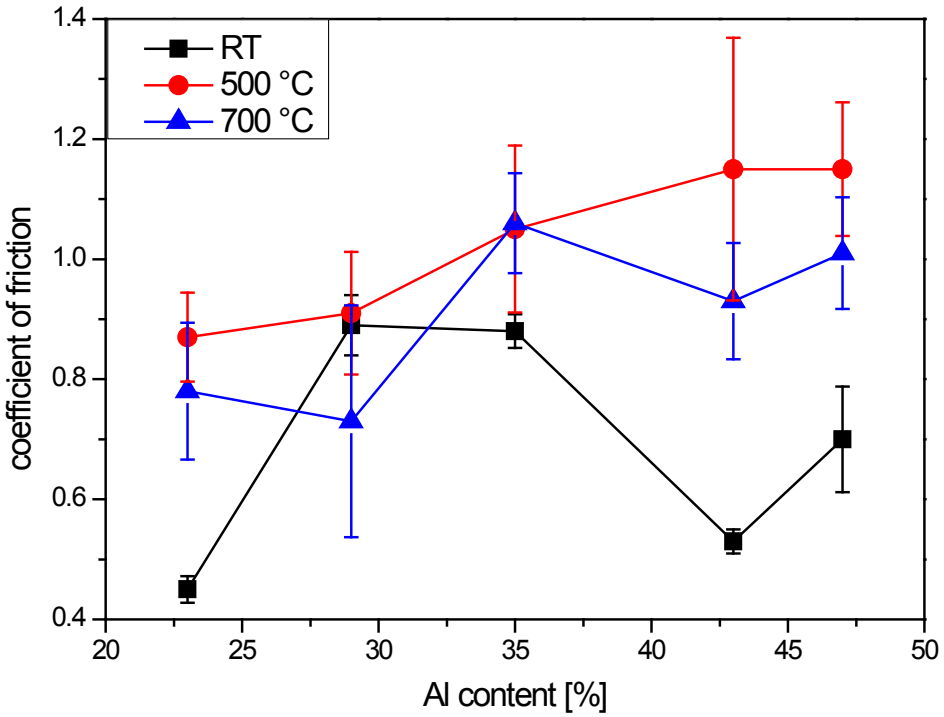

Fig. 5.19: Summary of the coefficients of friction measured at room temperature, 500 and 700 °C for $(Al,Cr)_2O_3$ coatings as a function of the Al content.

6 Summary and Conclusions

The aim of the present thesis was to deposit α–$(Al,Cr)_2O_3$ films with different chemical compositions on cemented carbide substrates. An industrial scale sputter plant has been equipped with special cathode shunts in order to use smaller sized, segmented targets provided by PLANSEE Composite Materials. Those segmented targets consist of two triangles which build a rectangle sized target when they are put together. One triangle was made of pure chromium and one of pure aluminum. To improve the film adhesion, a TiAlN base layer was added prior to the deposition of the $(Al,Cr)_2O_3$ film.

Special substrate holders were designed to mount every sample of the same geometry one upon the other, to deposit films with different chemical composition on every single sample.

Due to the target geometry and the arrangement of the samples on the substrate holder, a range of chemical compositions from chromium rich to aluminum rich would have been expected. In fact, the chemical investigations showed that there is less aluminum in the samples than estimated, aluminum contents from 22-49 at% were obtained. The unexpected low aluminum contents can be explained by the sputtering yields and the standard free energies of chromium and aluminum. On the one hand, aluminum has a lower sputtering yield compared to that of chromium and on the other hand aluminum builds more stable oxides which lead to partially more poisoned targets and consequently to less sputtered aluminum.

Measurements of the film thickness showed that at the lowest and highest deposited aluminum contents, which equal the lower and upper target borders, the film thickness decreases. That might be attributed to an increasing ion/neutral ratio at the upper and lower target borders. Since less film forming neutrals are available at those regions, the film thickness decreases.

In the whole range of investigated chemical compositions, a solid solution of $(Al,Cr)_2O_3$ was formed. The adhesion of the films on the cemented carbide samples was classified as moderate to bad.

The measured hardness of the films is in good agreement with literature and shows a strong dependence on the residual stresses. Increasing compressive residual stresses were detected on the lower and upper target borders. This consequently results in an increasing hardness in those regions. The determined values for the

Young´s modulus showed no dependencies on the residual stresses or on the aluminum content and correspond well to values for α–$(Al,Cr)_2O_3$ found in literature.

The lowest coefficients of friction were determined at the lowest aluminum contents and increase with increasing aluminum content. At 500 °C, the average coefficients of friction were slightly higher than the values measured at room temperature and at 700 °C. The examined wear tracks were either not very distinct or showed spallation of the film, thus it was not possible to determine wear coefficients. However, a good wear protective behavior of the films which did not delaminate can be expected on the one hand. On the other hand, the spallation of 5 out of 15 films indicates again a quite bad adhesion.

In conclusion, deposition of a solid solution of α–$(Al,Cr)_2O_3$ in an industrial scale sputtering plant was successfully done. The Al contents of the deposited coatings were unexpected low. Experiments with modified targets might lead to higher aluminum contents. Further investigations should pay attention to improve the adherence of the films, which might be possible by adding a booster etching step prior to deposition. For an economic industrial coating process, the deposition rate of ~0.125 μm/h for the segmented targets needs to be increased. Nevertheless, the films deposited within this work show a huge potential for wear exposed applications like parts in mechanical engineering and cutting applications.

Bibliography

[1] D. Hochauer, New high-performance oxide-based CVD coatings, PhD Thesis, Montanuniversität Leoben, 2010.

[2] R. Cremer, M. Witthaut, D. Neuschütz, G. Erkens, T. Leyendecker, M. Feldhege, Comparative characterization of alumina coatings deposited by RF, DC and pulsed reactive magnetron sputtering, Surf. Coat. Technol. 120-121, 213-218, 1999.

[3] D. Diechle, M. Stueber, H. Leiste, S. Ulrich, V. Schier, Combinatorial approach to the growth of α-$(Al_{1-x},Cr_x)_2O_3$ solid solution strengthened thin films by reactive r.f. magnetron sputtering, Surf. Coat. Technol., 204, 3258-3264, 2010.

[4] Fr.-W. Bach, T. Duda, Moderne Beschichtungsverfahren, Wiley-VCH, Weinheim, 2000.

[5] R. A. Haefer, Oberflächen- und Dünnschicht-Technologie, Teil I, Beschichtungen von Oberflächen, Springer Verlag, Berlin, 1987.

[6] B. Rother, J. Vetter, Plasmabeschichtungsverfahren und Hartstoffschichten, Deutscher Verlag für Grundstoffindustrie, Leipzig, 1992.

[7] R. F. Bunshah, Deposition technologies for films and coatings, Noyes Publications, New Jersey, 1982.

[8] M. Schulze, Physikalische Vorgänge in gepulsten Magnetronentladungen, Dissertation, Otto- von- Guericke- Universiaet Magdeburg, 2000.

[9] H. Frey, Vakuumbeschichtung 1, Plasmaphysik – Plasmadiagnostik – Analytik, VDI Verlag, Düsseldorf, 1995.

[10] D. M. Mattox, Physical Vapor Deposition (PVD) Processing, Elsevier Second Edition, Oxford, 2010.

[11] W.D. Sproul, D.J. Christie, D.C. Carter, Control of reactive sputtering processes, Thin Solid Films, 491, 1-17, 2005.

[12] P.H. Mayrhofer, Materials science aspects of nanocrystalline PVD hard coatings, PhD Thesis, Montanuniversität Leoben, 2001.

[13] M. Ohring, The materials science of thin films – deposition and structure, Academic Press, San Diego, Second edition, 2002.

[14] M. Moser, Structural evolution of protective coatings for gamma-TiAl based alloys, PhD Thesis, Montanuniversität Leoben, 2008.

[15] B.A. Movchan, A.V. Demchishin, Study of the structure and properties of thick vacuum condensates of nickel, titanium, tungsten, aluminum oxide and zirconium dioxide, Phys. Met. Metallogr. 28, 653-660, 1969.

[16] R. Messier, A.P. Giri, R.A. Roy, Revised structure zone model for thin film physical structure, J. Vac. Sci. Technol. A, 2(2), 500-503, 1984.

[17] J.A. Thornton, Influence of apparatus geometry and deposition conditions on the structure and topography of thick sputtered coatings, J. Vac. Sci. Technol. 11(4), 666 – 670, 1974.

[18] O Kyrylov, R Cremer, D Neuschütz, Deposition of alumina hard coatings by bipolar pulsed PECVD, Surf. Coat. Technol., 163-164, 203-207, 2003.

[19] J. Ramm, M. Ante, H. Brändle, A. Neels, A. Dommann, M. Döbeli, Thermal Stability of Thin Film Corundum-Type Solid Solutions of $(Al_{1-x}Cr_x)_2O_3$ Synthesized Under Low-Temperature Non-Equilibrium Conditions, Adv. Eng. Mater., 9, 604-608, 2007.

[20] M. Witthaut, R. Cremer, K. Reichert, D. Neuschütz, Preparation of Cr_2O_3-Al_2O_3 Solid Solutions by Reactive Magnetron Sputtering, Microchimica Acta, 133, 191-196, 2000.

[21] T. M. Besmann, N. S. Kulkarni, K. E. Spear, Thermochemical Analysis and Modelling of the Al_2O_3-Cr_2O_3, Cr_2O_3-SiO_2, and Al_2O_3-Cr_2O_3-SiO_2 Systems relevant to Refractories, J. Am. Ceram. Soc., 2006.

[22] J. Ramm, M. Ante, T. Bachmann, B. Widrig, H. Brändle, M. Döbeli, Pulse enhanced electron emission (P3e™) arc evaporation and the synthesis of wear resistant Al–Cr–O coatings in corundum structure, Surf. Coat. Technol., 202, 876-883, 2007.

[23] G. Kienel, Vakuumbeschichtung 3, Anlagenautomatisierung – Meß- und Analysentechnik, VDI Verlag, Düsseldorf, 1994.

[24] M. Birkholz, Thin film analysis by x-ray scattering, Wiley-VCH, Weinheim, 2006.

[25] B.D. Cullity: ‘Elements of X-ray diffraction’ 2nd ed., Addison-Wesley, Reading, Menlo Park, London, Amsterdam, Don Mills, Sydney, 1978.

[26] H.-R. Stock, A. Schulz, DIN-Fachbericht 39: Charakterisierung dünner Schichten, 1. Auflage, in H. Jehn, G. Reiners, N. Siegel, editors, Beuth Verlag, Berlin, 1993.

[27] R. Saha, W.D. Nix, Effects of the substrate on the determination of thin film mechanical properties by nanoindentation, Acta Mater., 50, 23-38, 2002.

[28] D. Winkler, Konzeption und Realisierung eines thermisch unterstützten Meßverfahrens zur Bestimmung von Eigenspannungen in dünnen Schichten, Diplomarbeit, Montanuniversität Leoben, 1997.

[29] J.F. Ziegler, M.D. Ziegler, J.P. Biersack, SRIM – the stopping and range of ions in matter, Version SRIM-2008.04, www.SRIM.org.

[30] L.S. Darken, R.W. Gurry, Physical Chemistry of Metals, McGraw-Hill, New York, 1953.

[31] T. Weirather, Hochtemperaturbeschichtung von $Ti_{1-x}Al_xN$ auf verschiedenen Schnellarbeitsstählen, Diplomarbeit, Montanuniversität Leoben, 2008.

[32] P. H. Mayrhofer, F. Kunc, J. Musil, C. Mitterer, A comparative study on reactive and non-reactive unbalanced magnetron sputter deposition of TiN coatings, Thin Solid Films, 415, 151-159, 2002.

[33] P. H. Mayrhofer, C. Mitterer, L. Hultman, H. Clemens, Microstructural design of hard coatings, Prog. Mater. Sci., 51, 1032-1114, 2006.

[34] T.Kohara, H. Tamagaki, Y. Ikari, H.Fujii, Deposition of α-Al_2O_3 hard coatings by reactive magnetron sputtering, Surface & Coatings Technology 185, 166-171, 2004.

[35] K. Pedersen, J. Bøttiger, M. Sridharan, M. Sillassen, P. Eklund, Texture and microstructure of Cr_2O_3 and $(Cr,Al)_2O_3$ thin films deposited by reactive inductively coupled plasma magnetron sputtering, Thin Solid Films, 518, 4294-4298, 2010.

[36] D. Hochauer, C. Mitterer, M. Penoy, C. Michotte, H.P. Martinz, M. Kathrein, Titanium doped CVD alumina coatings, Surf. Coat. Technol., 203, 350-356, 2008.

[37] Verband der keramischen Industrie, www.keramik-rs.de, 2011.